Development and deployment of a point-source digital inline holographic microscope for the study of plankton and particles to a depth of 6000 m

Alexander B. Bochdansky[1], Manfred H. Jericho[2], and Gerhard J. Herndl[3]*

[1]Ocean, Earth and Atmospheric Sciences, Old Dominion University, Norfolk, Virginia, USA

[2]Department of Physics and Atmospheric Sciences, Dalhousie University, Halifax, Nova Scotia, Canada

[3]Department of Marine Biology, University of Vienna, Austria & Dept. of Biological Oceanography, Royal Netherlands Institute for Sea Research (NIOZ)

Abstract

A point-source digital inline holographic microscope (DIHM) was designed for the imaging of particles from 50 µm to several millimeters in size. The DIHM operates autonomously without connection to external recording devices or power sources and delivers 4.2 megapixel images at a rate of approximately 7 images s^{-1}, each image representing a snapshot of 1.8 mL seawater. Reliance on largely off-the-shelf components, and simplification in its construction makes this camera system adaptable to various particle size ranges and environments, and easy-to-operate for nonexpert users. The DIHM produced sharp images of protists with skeletal structures (e.g., acantharians, tintinnids, dinoflagellates), mesoplankton (e.g., copepods, appendicularians, medusae), *Trichodesmium* colonies and marine snow particles while descending in the water column at 1 m s^{-1}, a typical velocity for deployments of tethered instruments and samplers from oceanographic vessels. To validate the usefulness of the new instrument in an oceanographic context, data are presented of the surface distribution of *Trichodesmium* spp., and of the vertical frequency distribution of fecal pellets and other particles in the deep sea. The point-source DIHM has the potential to become a standard instrument on the CTD rosette (i.e., on the basic oceanographic instrument and sampling frame) in the future providing a permanent archival record of the water column that can be mined for specific target particles in the future.

The application of holography for imaging plankton organisms has a long history from initially those based on individual photographic plates to most recently those based on CCD and CMOS sensors (Knox 1966; Beers et al. 1970; Solokov et al. 1971, Malkiel et al. 1999, 2006; Watson et al. 2003; Watson 2005; Sun et al. 2007; Jericho et al. 2006, 2010; Lewis et al. 2006; Xu et al. 2001). Holography has been used in different embodiments either in its simplest form as Fraunhofer inline holography or off-axis holography (Vikram 1992). Lacking lenses that require focusing on an image plane, its primary appeal is the inherently large depth of field of individual images. This allows holography to image volumes of water that are orders of magnitude larger than those obtained through conventional lens technology. The ability to reconstruct size and position of objects in the three-dimensional space has led to a large number of applications from behavioral studies of zooplankton (Heflinger et al. 1978), sediments (Black et al. 2001, Perkins et al. 2004, Sheng et al. 2006), air bubbles (O'Hern et al. 1988), and settling particles (Carder et al. 1982, Graham and Nimmo Smith 2010). Systems for the study of plankton include freely-drifting and towed holographic cameras (Katz et al. 1999; Pfitsch et al. 2005; Sun et al. 2007), some of which are already commercially available (LISST-HOLO, Sequoia Scientific Inc.), and some of which are under development ("Holosub," Talapatra et al. in press).

Here, we will introduce a newly designed instrument that can easily and affordably be assembled from off-the shelf components. The two cylindrical underwater housings (one for the light source and one for the camera) can be customized for any desired depth range by simply changing wall thickness and materials. This flexibility in assembly was possible due to the rapid and recent development in electronics such as high resolution megapixel machine view cameras, GigE speed communication links between camera and recording device, large storage capacity of SATA hard disks, improved writing speeds

of hard drives, and miniaturization of embedded computers with conventional software that can be programmed by non-expert users. We describe our design innovations and software integration and illustrate our experience during the first oceanographic deployment in the tropical and subtropical Atlantic to a maximum depth of 6000 m, by far the deepest deployment of any holographic camera to date.

Materials and procedures

The hardware items required for the DIHM consisted of a 640 nm diode laser (Dragon Lasers, Spartan Series), a gradient index (GRIN) lens to serve as a beam collector for a single mode fiber, a mode scrambler (simply consisting of four pins embedded in an aluminum block that forced sharp turns on the optical fiber), a 4.2 Megapixel (2048 × 2048) dual-tap Gigabit Ethernet progressive scan camera (model Pulnix, TM-4200GE, JAI), an eBOX530-820-FL1.6G-RC computer (Axiomtek) with Gb LAN to connect to the camera through a Cat6 Ethernet cable, and a 750 GB hard disk to record images (Fig. 1). The 100 mW laser in our setup was too powerful and needed to be attenuated by slight misalignment of the fiber optics assembly (this undesirable method of adjustment was recently replaced by direct voltage control of the laser). We used rechargeable nickel-metal hydride (NiMH) battery packs (BatterySpace.com/AA Portable Power Corp.) customized to best use available space in the pressure housings (4.8 V for laser and computer, 12 V for the camera). NiMH batteries are safer than lithium batteries (thus can be shipped as nonhazardous material), and do not suffer voltage depression ("memory effect") as noticeably as rechargeable nickel-cadmium batteries. Although the camera can theoretically deliver 15 frames per second, the image processing and writing speed of the SATA hard drive limited the recording speed of the capture software (Streampix, Norpix) to ca. 7 frames per second. The

instrument housings consisted of two cylinders made of 316-stainless steel (each: length = 41 cm, outer diameter = 15 cm, wall thickness = 19 mm), and were facing each other with their optical ports. Four stainless steel dowel rods, held in place with set screws, maintained a straight optical axis and set the distance between the two housings (Fig. 1). The dowel rods were offset sideways to leave a 9 cm wide and 7 cm deep channel for vertical water flow. The optical ports were made of sapphire (Meller Optics). The sapphire was 3 mm thick at the point source and covered an unsupported diameter of 1 mm, and was 11 mm thick at the camera port and covered an unsupported diameter of 10 mm (Harris 1992). A thin window is particularly important at the point source (i.e., the fiber optics) because the closer the object is to the point source the higher its resolution. As a consequence, the smallest organisms described here can only be seen close to the point source window, whereas whole bodies of larger organisms may be imaged at larger distances albeit at lower resolution. Since we used a fiber optic filament, we were able to reduce the hole in the stainless steel casing (i.e., the unsupported diameter of the sapphire window) to 1 mm. The three millimeter thickness of the sapphire window is conservative and thinner windows may also work depending on the evenness of the stainless steel face and impurities contained in the sapphire (Harris 1992; Chervin et al. 1994). The total distance between point source and camera chip was 121 mm, of which 70 mm was through seawater. The active area of the chip was 15.15 × 15.15 mm (JAI). The sapphire windows were sealed with single O-rings in face-seal glands. The end caps (5 cm thickness) had single O-rings in male static-seal glands. The housings were mounted on the lowest point in the center of the CTD rosette with high-density polyethylene mounting brackets leaving an unobstructed path for the water to flow from bottom up between the housings (Fig. 2).
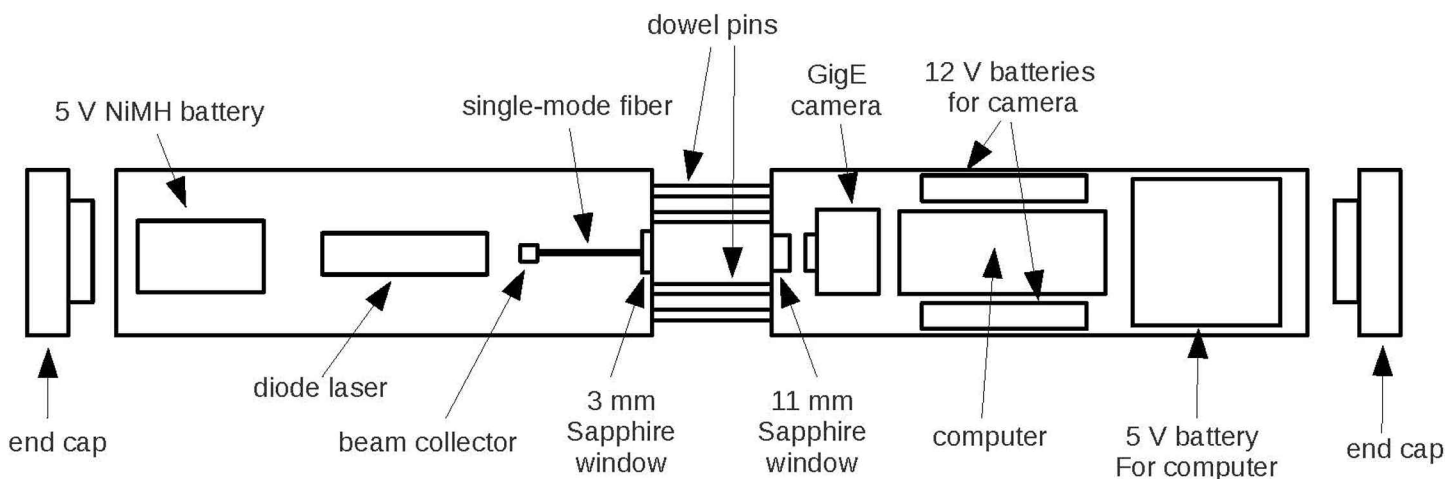

Fig. 1. Lateral schematic of the cylindrical stainless-steel camera housings connected with four dowel pins. The interior arrangement separated the chambers into a light-emitting and light-receiving compartment separated by a 7 cm image gap. The point source was red laser light projected from a 125 μm diameter single-mode fiber onto a 15.15 × 15.15 mm chip of a progressive scan GigE camera. The videos were recorded by an embedded computer with a 750 GB hard drive connected through a Cat6 Ethernet cable. Individual NiHM batteries supplied power for laser, camera, and computer.

Fig. 2. Mounting of the DIHM on the CTD frame (a) and close up of the camera port reflecting the red laser light (b). The overall length of the DIHM is 137 cm.

The empty casings were pressure tested to 703 bar within 25 min, held at this pressure for 1 h, and returned to atmospheric pressure within 20 min. Measurements of the inside of the instruments housings revealed a permanent deformation of the diameter at the center of both cylinders by 0.5 mm. The housings were thus not deployed beyond 6000 m in our field trials. However, a depth range of 6000 m is sufficient to reach bottom depths of 98% of the total area of the ocean (i.e., the entire world's ocean except for hadal-pelagic regions).

Only videos from the downcast were used for analysis in order to avoid disruptive turbulence from the CTD cage and attached instruments during the upcast. The circular image touched the edges of the frame of the 15.15 × 15.15 mm chip. The theoretical maximum image volume of 1.8 mL was thus calculated using the formula of a cone ($V = \pi/3r^2h$) where r is the cone radius at the outside the sapphire window and h the distance from the point source to the outside the sapphire. In this calculation, the volume inside the sapphire at the point source is small enough to be ignored. This, however, is a theoretical maximum image volume that cannot be maintained for particle sizes smaller than 50 μm (see below).

The total number of frames for the recording was set prior

to deployment to cover at least one entire downcast period. It was important that the sequence was finished and closed before battery power was depleted to avoid corrupt video files. Since the outside of the instrument cools to less than 2°C during descent through the deep ocean, some allowance must be given for weaker battery capacity and the increase of light emittance of the diode laser when cooled to deep-sea temperatures. Videos were viewed with the Streampix3 software and individual frames were saved as bitmap files for reconstruction. Because the camera was a progressive scan-type, no interlacing of half frames was necessary. A time stamp and frame number was automatically assigned by the software to the bitmap file name in order to relocate the image in the sequence later, and to correlate the individual images with depth. The internal clock of the PC was later matched with the CTD computer to 1 s accuracy to assign exact depths to each image. Synchronization time point was when the camera entered the water, which was clearly visible in the raw videos. Image reconstruction was done on individual frames. These frames were selected from the video stream manually by pausing whenever a visible object appeared. These unreconstructed holograms appeared as interference patterns with concentric circles emanating from the object (Fig. 2). A reference image close to the object image in the sequence but without particles was also saved (Xu et al. 2002). Pixel-by-pixel subtraction of such a reference hologram from a hologram that contains an object produces what is called the contrast hologram. This subtraction procedure helps to correct for imperfect laser illumination (such as object illumination with imperfect spherical waves) and eliminates from the images the effects of fixed dirt particles on the sapphire windows. Reconstructions of contrast holograms generally produced the best object images.

Once a series of bitmap images were stored, contrast images were prepared and reconstructed using DIHM reconstruction software (Holosuite, Resolution Optics). The holograms were reconstructed by initially stepping through the holograms manually in 1-2 mm steps. Whenever an object appeared in more detail, step-size was reduced to 0.1 mm for fine tuning. With a high-speed video card such as used in gaming computers (e.g., a GeForce model GTX 560 Ti), up to 7 images can be reconstructed per second allowing for a smooth focusing on particles of interest similar to turning the focus knob on a conventional microscope. There are several settings that needed to be entered into the software for accurate reconstruction: pixel size of the camera (7.5 μm), the number of pixels (2040 × 2048), the effective size of the CCD chip (15.15 × 15.15 mm), the wavelength of the laser (640 nm), the distances of the light path in the three media and their respective indices of refraction at 640 nm (air: $n_a = 1$, seawater: $n_{sw} = 1.33$, and sapphire: $n_s = 1.76$) in order to calculate the effective wavelength (Jericho et al. 2006).

The principles of digital inline holography and image reconstruction algorithms were published previously (Gabore 1948; Kreuzer et al. 1992; Xu et al. 2001; Xu et al. 2003; Jeri-

cho et al. 2006). Briefly, light from a laser is focused onto a pinhole, or in this case, one end of an optical fiber. The other fiber end acts as a "point source" from which a nearly spherical wave emanates. This wave illuminates objects that scatter a small portion of this light. The scattered light and the unscattered portion of the illuminating spherical wave then combine at a screen to form a geometrically magnified interference pattern or hologram. A hologram is generally speaking a complex two-dimensional pattern of overlapping fringes. To view the objects that are encoded in the hologram, the hologram has to be reconstructed with suitable computational methods. The role of reconstruction is to obtain the three-dimensional structure of the object from the two-dimensional hologram on the screen, or, in physical terms, to reconstruct the wave front at the object. Reconstruction is performed in selected planes throughout the imaged volume so that a reconstruction plane in the DIHM is equivalent to an in-focus plane in conventional microscopy. For the implementation of hologram reconstruction we employed the Kirchhoff-Helmholtz transform (Xu et al 2002). The fundamental equation of the image reconstruction algorithm is

$$K(\vec{r}) = \int_S d^3\xi \tilde{I}(\vec{\xi}) \exp[i2\pi\vec{\xi} \cdot \vec{r} / \lambda\xi] \tag{1}$$

where K(r) is the Kirchhoff-Helmholtz transform function and the integration extends over the two-dimensional surface of the chip with coordinates ξ = (X,Y,L), and where L is the distance from the point source (fiber end) to the center of the chip and λ is the wavelength of light emanating from the point source. I(ξ) is the contrast image and the function K(r) is different from zero only in the space region occupied by the object. The Kirchhoff-Helmholtz transform for reconstruction of point source holograms was first introduced by Kreuzer et al. (1992).

In holography, which depends on phase shifts and interference of light, and if the space between point source and screen is filled with water, the interference pattern on the screen is thus formed with light of shorter wavelength and will generally show more fringes and hence better resolution. When light travels through several media, each with its own refractive index, the interference pattern on the screen (i.e., the hologram) is determined by an effective wavelength (Jericho et al. 2006) that depends on how far light travels in each medium and can be calculated with the formula

$$\lambda_{eff} = \lambda D/(s_1 n_1 + s_2 n_2 + \ldots\ldots s_j n_j) \tag{2}$$

where D is the source – screen distance and s_j the length of the optic path with refractive index n_j.

To assess the usefulness of the DIHM for particle characterization and enumeration, we performed two types of analysis: 1) enumeration of *Trichodesmium* spp. colonies (both tufts and puffs were identified, Davis and McGillicuddy 2006) in the surface in a horizontal transect over a large area of the sub-

tropical North Atlantic, and 2) enumeration and sizing of approximately 6000 particles (divided into fecal pellet-type particles and all others) in vertical profiles through the water column to a maximum depth of 6000 m. For the determination of *Trichodesmium* colony numbers (1), the CTD frame was submerged just below the surface with the camera being located 2-3 m below surface (oscillations due to the swell and roll of the ship). Images were recorded for approximately 2 min with the total observed volume being determined by multiplying the volume of each image (1.8 mL) by the number of frames per second (7 Hz), and by the total recording time (s). For the deep-sea particle analysis (2), numbers were pooled according to the water mass definitions in Tomczak and Godfrey (2003) and pairwise comparisons among the water masses were performed. The water masses were defined as follows: Antarctic Intermediate Water (AAIW, depth range: 250–1500 m, neutral density: 27–27.8, temperature: 7.2 ± 2.3°C), North Atlantic Deep Water (NADW, depth range: 1600 – 4000 m, neutral density: 27.98–28.14, temperature: 2.5 ± 0.5°C), and Antarctic Bottom Water (AABW, depth range: 4000–6000 m, neutral density: 28.14-29.00, temperature: 1.4 ± 0.5°C).

Assessment

The camera was deployed 20 times on the R/V *Pelagia* during the MOCA research cruise to the subtropical and tropical Atlantic between 10.72°N-26.59°N and 17.56°W- 44.67°W. The most conspicuous large particles in the upper ocean such as *Trichodesmium* colonies (Fig. 3), metazoan plankton such as medusae, copepods, and appendicularians all produced excellent images (Fig. 4). Among protist plankton, we found only larger ones reliably identifiable, and only those that had skeletal parts such as large dinoflagellates, tintinnids, and acantharians (Fig. 5). Some larger structures such as the colonies of *Trichodesmium* could often be recognized even from the unreconstructed holograms (Fig. 3). Each of the *Trichodesmium* trichomes were 5 to 8 µm in width (LaRoche and Breitbarth 2005), which is at the lower range of the resolution of our setup. It was also possible to obtain high resolution images of detrital and amorphous marine snow particles at high resolution providing insight into their composition and thus potential sinking speed (Fig. 6). For instance, a particle cluster composed of optically dense strings weighted by large ovoid fecal pellets will sink very quickly through the water column (Fig. 6c). When these types occur at high frequency, they indicate high export fluxes from the euphotic zone to the deep sea. However, large clusters of small particles embedded in an invisible mucous matrix are very likely to sink slowly if at all (Fig. 6f). These clusters (Fig. 6f) may be a result of production and aggregation at depth and, because they are colonized by large numbers of microbes, leave a permanent imprint in the oxygen record of specific deep-sea water masses (Bochdansky et al. 2010). The DIHM makes it possible to examine in detail the composition and characteristics of these marine snow
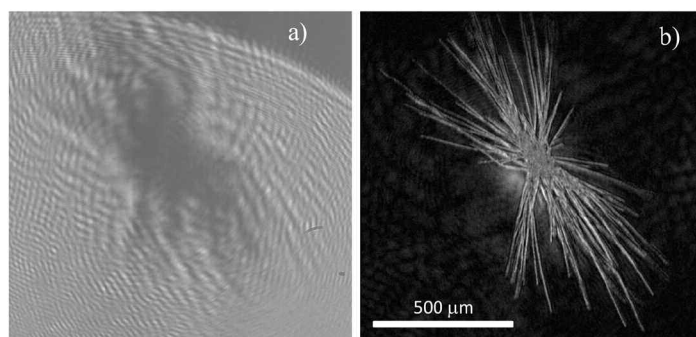

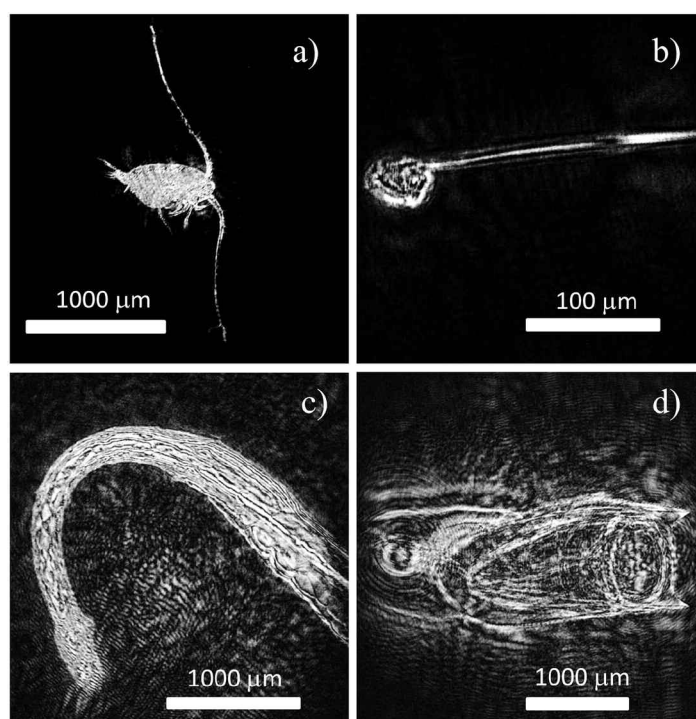**Fig. 3.** *Trichodesmium* sp. puff as unreconstructed original image (a) and after reconstruction (b).

Fig. 4. Metazoan plankton as imaged by the DIHM: a) copepod, b) appendicularian, c) chaetognath, d) siphonophore.

particles, which are very important for biogeochemical fluxes in the ocean. Since these particles are very fragile, no sampling method based on Niskin bottles or plankton tows would be able to retrieve them intact, or display them in their full fractal geometry.

Many small particles were reconstructed, most likely protists and small fecal pellets, but the resolution was insufficient to identify them in more detail. However, size measurements of their maximum linear dimension were still possible (Fig. 7). Nanoplankton (<20 µm), such as heterotrophic flagellates, and picoplankton (<2 µm), such as bacteria, are out of reach of this particular setup as they do not produce sufficiently strong fringe patterns to create an image. The high resolution
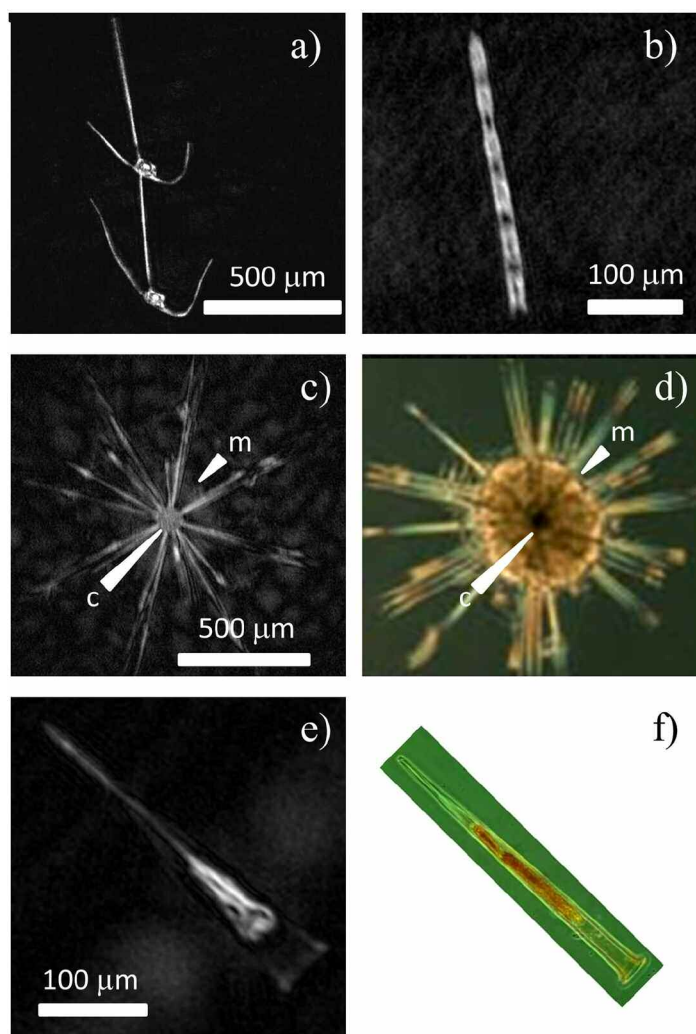
Fig. 5. Microplankton: a) two individual cells of *Ceratium* sp. (Dinoflagellata), b) a diatom chain, c) an acantharian species [c = inner capsule, m = extent of the cell body], d) similar acantharian species as seen under the phase contrast microscope for comparison (c and m as in Fig. 5c; image courtesy of David Patterson licensed to MBL at micro*scope: http://starcentral.mbl.edu/microscope/), e) a tintinnid, f) a tintinnid as seen under the phase contrast microscope for comparison (image by John Dolan licensed to MBL at micro*scope: http://starcentral.mbl.edu/microscope/).
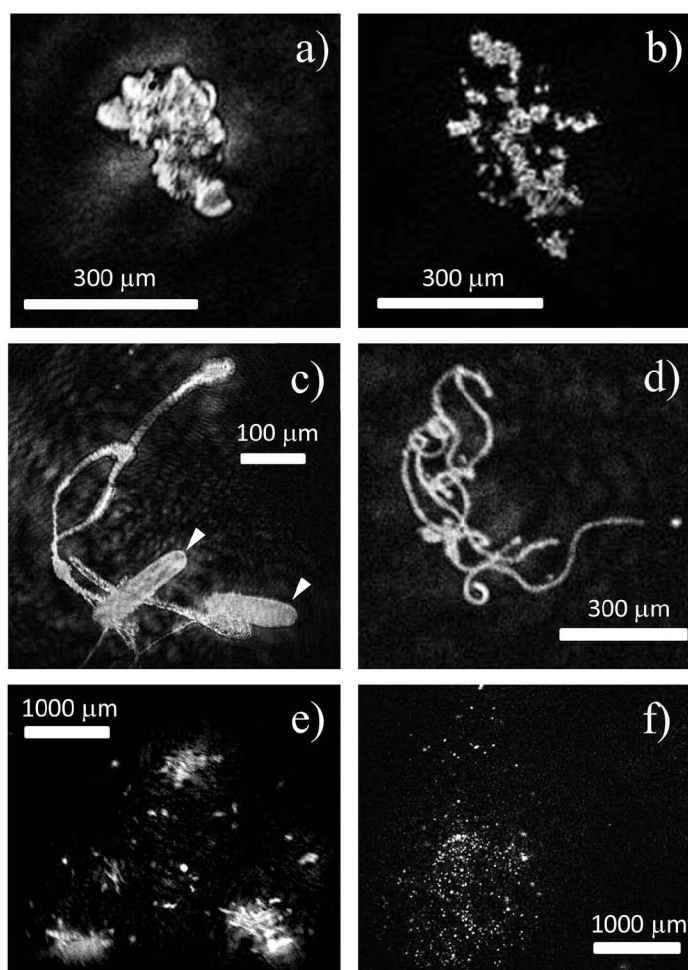
Fig. 6. Marine snow particles: a) small solid particle, b) small porous particle, c) strings ballasted with two ovoid fecal pellets (arrows), d) strings (possibly a colony-forming organism or a fecal string), e) particles connected with invisible matrix, f) small particles embedded in a large amorphous matrix. Particles shown in b), e), and f) may sink slowly or may be neutrally buoyant whereas a), c), and d) are more likely to sink quickly through the water column.

configuration for DIHM imaging normally used for bench-top measurements could not be realized in the deep-sea instrument because of the constraints imposed by the thick walls of the pressure chamber so that the CCD chip could not be placed immediately behind the sapphire window. Bench tests with a variety of objects that ranged from 5 μm to several hundred μm in size showed that, under static water conditions, a better than 5 μm resolution was obtained for objects within about 10 mm of the point source. At larger distances the resolution degraded. The inability of the deployed instrument to reconstruct objects < 50 μm reliably over the entire light path is most likely due to the 1m s^{-1} flow rate of the water column

that would tend to wash out the fringe pattern of an object during the 62.5 μs minimum exposure time of the CCD camera. This is particularly true for particles that are both small and transparent. On the other hand, for larger and more opaque structures, such as the chitin skeletons of copepods, the resolution limit was much lower (i.e., slightly better than 5 μm, Fig. 8).

The Holosuite program was also used for sizing of organisms using the "image cut" function. For the standard DIHM configuration (source – screen distance of about 20 mm), the program is designed to directly calculate the distance of a reconstruction plane from the point source as well as the lateral scale in the reconstruction plane. For the deep sea instrument, with its much larger imaged distance (i.e., 70 mm), the numbers calculated by the Holosuite program for source
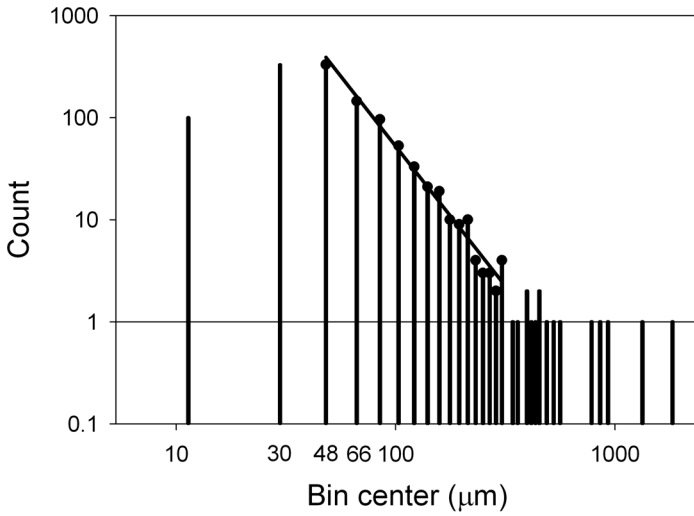
Fig. 7. Particle size frequency distribution of 1188 particles from 100 to 578 m at one station in the subtropical Atlantic (13°38.14'N, 34°43.74'W, 16 Oct 2010). The regression equation over the linear portion of the frequency distribution is *counts* = 7.197 × $D^{-2.74}$ (*n* = 15, *r* = 0.973, *P* < 0.0001), where *counts* is the number of particles at each size bin, and *D* the center of the bin (of 100) of the longest dimension of the particles. Particles of less than 50 μm in maximum length are not reliably captured by this DIHM setup.

Fig. 8. Example of the capability of the DIHM to produce high-resolution images despite a 1 m s^{-1} speed through the water. The insert shows a magnified detail from the white rectangle in the main image (i.e., sensory hairs on the left antenna of a cyclopoid copepod). The image moved by less than 3 pixels.

–object distance and object size had to be corrected. The calibration was performed on a lab bench with a system that had an optical path identical to that of the actual instrument. The calibration probe used was a 148 μm diameter wire that was positioned in the water section along the optical path at measured distances. In our specific setup, the actual distance of the object from the point source (mm) was best calculated using the fourth-order polynomial:

$$D_{cor\ r} = -7.76 \times 10^{-8} \times D_m^4 + 3.68 \times 10^{-5} \times D_m^3 - 7.77$$
$$\times 10^{-3} \times D_m^2 + 1.078 \times D_m + 2.3 \times 10^{-4}, \quad (3)$$

where D_{corr} is the corrected distance from the point source (mm) and D_m the distance from the point source (mm) as determined by the Holosuite program.

The corrected size (μm) of the object (S_{corr}, mm) was calculated by the equation:

$$S_{corr} = S_m \times (1 + 8.93 \times 10^{-3} \times D_m)^{-1}, \quad (4)$$

where S_m is the size (μm) as determined by the program.

It is prudent to perform this calibration with objects of known sizes such as beads, stage micrometers, or wires for every specific setup. Based on these corrections, and in order to provide an example, a size distribution of 1188 particles was determined for one station and one depth range (Fig. 7). We know from first principles that the number of particles per bin position will increase exponentially when the bin center is moved in the direction of smaller particle size (e.g., Jackson et
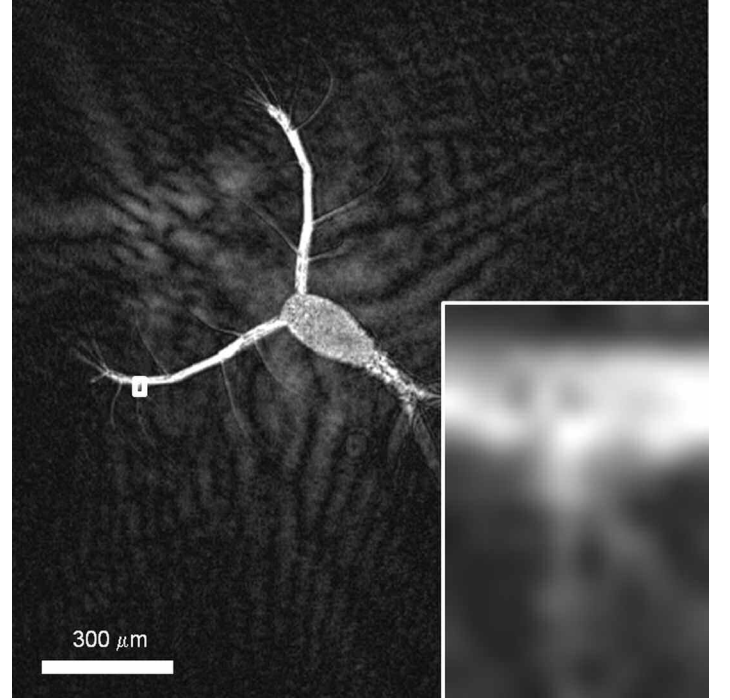
al. 1997). A drop in the measured number of particles below that expected from an exponential increase indicates the limit of reliable detection in this particle size range. In our particular setting, the smallest size reliably enumerated with the DIHM was 50 μm with smaller particles being underrepresented (Fig. 7).

The concentration of *Trichodesmium* colonies in the surface layer determined along the cruise transect through the tropical and subtropical Atlantic is shown in Fig. 9. The colony concentrations ranged from 2000 to 20,000 colonies m^{-3} with a mean of 7097 m^{-3} (SD = 5062, 13 stations). Of these, an average of 48% of the total colonies were tufts (SD = 27%) (Davis and McGillicuddy 2006).

Particle data in the deep sea were grouped according to water masses (i.e., Antarctic Intermediate Water, North Atlantic Deep Water, and Antarctic Bottom Water) and divided into those that had a distinct fecal pellet shape and "others." Frequency distributions of maximum lengths of particles are shown for each water mass in Fig. 10. Below a length of 50 μm, numbers drop off because small particles cannot be reconstructed across the entire optical path (Fig. 10, also see Fig. 7). Particles larger than 50 μm can be reliably counted and absolute numbers per volume are available for sizes up to several millimeters depending on the total volume surveyed. The results of Kolmogorov-Smirnov two sample tests of the distributions in Fig. 10 are presented in Table 1.
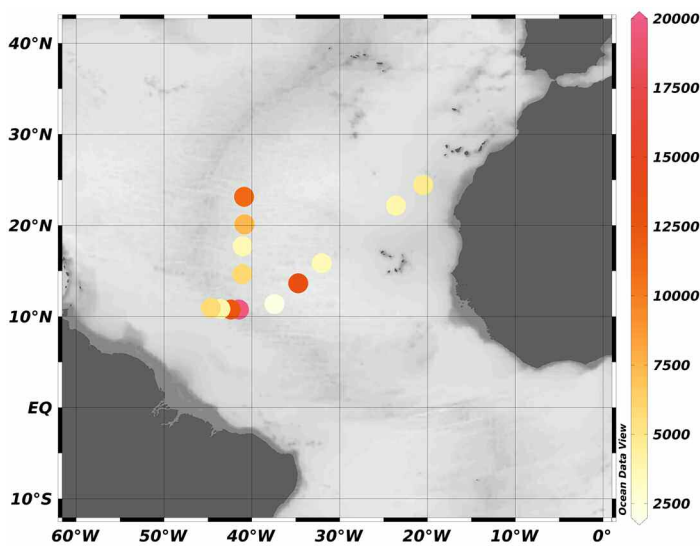
Fig. 9. Surface plot of number of *Trichodesmium* spp. colonies (numbers m⁻³) in the subtropical Atlantic during the Archimedes IV research expedition (9 Oct- 4 Nov 2010). Images were taken while the instrument was kept at the surface (camera depth 2-3 m) for approximately 2 min.

Discussion

This is the first time a holographic microscope was deployed to 6000 m water depth, and the first time it was used as part of routine CTD rosette deployments. In conventional optical microscopy, high magnification objectives produce images with only a narrow plane of focus (~ a few μm for a 40 × objective). In contrast, the DIHM can capture information from objects suspended in the illuminated volume over distances of more than a decimeter. This makes the DIHM particularly useful for the imaging of particle suspensions or organisms that occur at low abundances as is typical for oligotrophic marine environments. With the setup as shown here, and deploying the instrument to the average ocean depth of 4000 m at a speed of 1 m s⁻¹, a total volume of 50 L can theoretically be interrogated. Whereas 50 L may not seem much, this volume is many orders of magnitude greater than using a lens-based system. In other words, if one were to mount a standard microscope on a CTD frame and lower it to the average global ocean depth of 4000 m, one may not capture one single organism while the DIHM yields thousands of images of organisms in their natural state and position. Furthermore, fragile particle assemblages, such as marine snow, are being imaged in a relatively undisturbed state, whereas they cannot be collected with plankton nets without disintegration (Fig. 6). The setup presented here can be adjusted over a wide range to optimize the detection of smaller and larger particles by decreasing or increasing the imaging gap, respectively, between point source and camera. New holographic imaging systems such as the Holosub (Talapatra et al. in press) can image even larger volumes and may be better equipped to
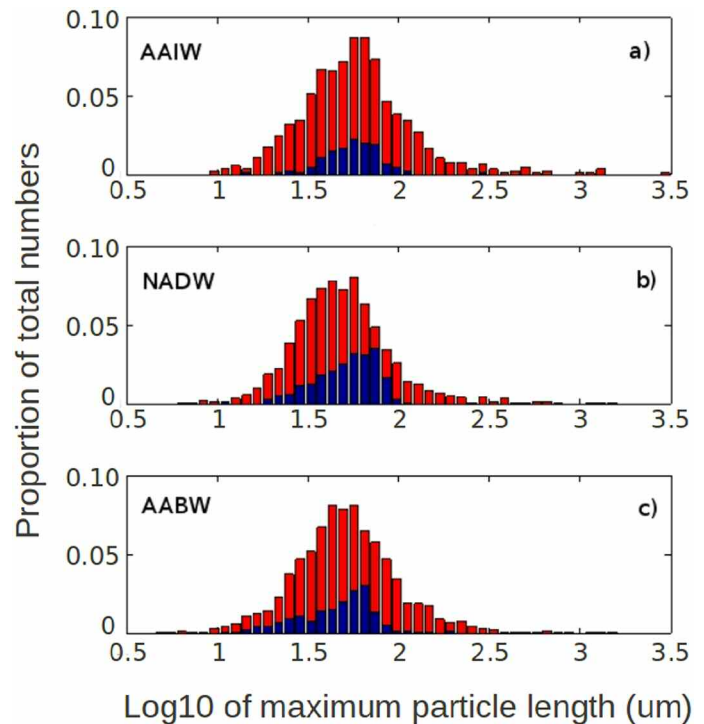

Fig. 10. Relative particle size spectra using the maximum linear dimensions (μm) of deep-sea particles of 6000 individual images as determined by the DIHM in the three dominant water masses of the North Atlantic according to the classification of Tomczak and Godfrey (2003). AAIW = Antarctic Intermediate Water 250 – 1500 m (a), NADW = North Atlantic Deep Water 1600 – 4000 m (b), AABW = Antarctic Bottom Water 4000 – 6000 m (c). The particles were grouped into fecal pellet-type particles and into all others. The total number of particles in each panel is normalized to 1. Blue bars: fecal pellet-type particles; Red bars: all other shapes. The results of all pairwise comparisons between the frequency distributions using Komolgorov-Smirnov statistics are shown in Table 1.

visualize fine-scale spatial distribution of particles such as found in thin-layers (McManus and Woodson 2012), where integration over a large number of holograms may not be possible. Parallel beam digital holography (Katz et al. 1999) has the additional advantage over a point source digital holographic microscope in that resolution is constant along the image beam. In the latter, the resolution of the reconstructed image depends on the distance between the point source to the object, the source to screen distance, the screen and pixel sizes, and the speed at which the water moves creating a certain degree of motion blur that changes with distance from the point source. The resolution of images is highest for objects that are closest to the point source and decreases with distance from it. Larger organisms, on the other hand, can only be fully imaged when they are smaller than the cross-sectional area of the image cone. However, high resolution is not as important for the identification of larger organisms as it is for smaller organisms. The maximum size that can be imaged with our setup is equivalent to the diameter of the light beam closest to the camera and is slightly smaller than 1 cm.

Table 1. Comparison of the particle size distributions (maximum linear dimension) of particles for the three major deep-sea water masses of the North Atlantic (Fig. 10). "Other particles" are all particles combined including live zooplankton and amorphous marine snow that do not have the characteristic shapes of fecal pellets. A Kolmogorov-Smirnov two sample test revealed that the frequency distributions of particles in the different water masses were significantly different in all but two instances. n = number of reconstructed and analyzed particles for each of the water masses; P = probability of the null hypothesis that the particle-size distributions come from the same statistical populations.

Type of particles	Water masses	n	K-S statistic	P
"Other" particles (Fig. 10, red bars)	AABW versus NADW	2160 + 1066	0.0632	0.0063
	NADW versus AAIW	1066 + 723	0.1485	<0.0001
	AABW versus AAIW	2160 + 723	0.0938	0.00013
Fecal pellets (Fig. 10, blue bars)	AABW versus NADW	469 + 310	0.1372	0.0016
	NADW versus AAIW	310 + 110	0.1419	0.0689 n.s.
	AABW versus AAIW	469 + 110	0.2065	0.00081
All particles	AABW versus NADW	2629 + 1376	0.0391	0.1234 n.s.
(total)	NADW versus AAIW	1376 + 833	0.1288	<0.0001
	AABW versus AAIW	2629 + 833	0.0987	<0.0001

Although larger flagellates may fall within detectable size ranges, we did not find a single recognizable cell. Given that there are at least 10^5 bacteria mL^{-1} (1.8×10^5 per image volume) and approximately 10^3 flagellates mL^{-1} (1,800 per image volume) in the surface waters of the tropical ocean, it is obvious that neither of these groups of organisms were detectable with the settings we used here. Many flagellates exceed 5 µm in size (i.e., the lower detection threshold of structures we were able to image such as setae of copepods, and individual *Trichodesmium* strands). Thus objects of sizes less than 50 µm linear dimension seem to require a minimum opacity or refractive index to produce an interference pattern in the hologram. In the case of the cantharian, the cell protoplasma, which is visible in phase contrast light microscopy left only a light halo in the DIHM image whereas hard structures were clearly visible in the DIHM image (Fig. 5c,d). Also, the only visible ciliates were tintinnids and not aloricate forms that are usually more numerous. We thus conclude that microplankton lacking hard structures and with refractive indices close to water cannot be imaged with the current setting. However, because of their larger sizes, appendicularians, medusae, and marine snow imaged well despite their transparency. It is interesting to note that during bench testing of the deep-sea optical system, objects down to 10 µm in size (*Tetraselmis* sp. algae) were clearly imaged at flow rates of 0.04 m s^{-1}, but with much shorter source - camera distances (data not shown).

Color cannot be reproduced with the DIHM because inherently, only monochromatic light can be used. The same holds true for shadow images created by collimated light such as in the video plankton recorder or similar setups (Davis and McGillicuddy 2006; Bochdansky and Bollens 2004). However, lack of color reproduction is a secondary problem for practical reasons as color has traditionally not been used for identification of plankton simply because most colors bleach when organisms are stored in preservatives.

The size of the holographic camera presented here is comparable to the eHolocam (Sun et al. 2007) but larger and heavier than a tethered drifting submersible holographic system (Pfitsch et al. 2005) mainly because of the weight of its pressure housings. Both cameras (Pfitsch et al. 2005; Sun et al. 2007) are set to larger size ranges that record larger volumes albeit at lower resolutions. In contrast to other systems, we also found that a light-weight diode laser is preferable over the more complex, power-hungry and heavier Neodynium solid state lasers.

Other plankton imaging systems that should be mentioned here and that are not based on holography are the video plankton recorder (Davis et al. 1992a,b) and the FlowCytobot (Sosik and Olson 2007). The video plankton recorder is based on collimated light that produces shadow images of objects on the screen and also set to larger image volumes at lower resolution. The FlowCytobot is a high resolution imaging system that allows for the taxonomic identification of individual algal cells and coupling with individual flow cytometry signals. The depth of field and orientation problem in this lens-based system was overcome by providing a sheet fluid that aligns the algae in a specific orientation and at an optimal distance from the lens (Sosik and Olson 2007). The FlowCytobot system, however, is limited by comparably small image volumes, and thus not able to image larger amorphous marine snow particles.

Due to the fast shutter speeds (62.5 µs), ambient light did not interfere even in the sunlit surface waters of the tropics at noon. Thus we were able to image surface plankton without the need of light shielding that could have interfered with the free flow of water through the imaging gap. Optical systems relying on strobes of light may not be able to perform as well under these bright light conditions unless the shutter speed of the camera is kept equally short and synchronized with the laser pulse. A combined strobed laser–high shutter speed approach would accommodate even higher towing speeds, however, would also significant increase complexity and costs of the system.

Trichodesmium spp. is the most important nitrogen fixing organism in the open ocean. Its contribution is sufficiently large so that whole ocean basins shift from nitrogen to phosphorus limitation due to its activity (Wu et al. 2000). To better understand its contribution to the biologically available nitrogen pool with anthropogenically fixed nitrogen on the rise (Gruber and Galloway 2008), their basin-scale enumeration is important. The colonies are imaged exceptionally well with the DIHM (Fig. 3) and thus can be reliably enumerated using this method. The surface concentrations of *Trichodesmium* spp. colonies (Fig. 10) fall within the wide ranges reported for the tropical and subtropical Atlantic (Tyrrell et al. 2003; Carpenter et al. 2004; Davis and McGillicuddy 2006). Their abundances ranged widely (approximately 2000–20,000 m^{-3}) even among stations relatively close to each other (Fig. 9). Even higher variability is apparent to any shipboard observer who can see patches and bands of *Trichodesmium* colonies in the clear subtropical water. To better assess the small scale variability in colony numbers, a towed deployment of the DIHM similar to the Video Plankton Recorder (Davis and McGillicuddy 2006) or a configuration attached to ship's hulls is conceivable.

Even a simple distinction between types of particles of the deep sea can help in the interpretation of source of particles and their potential sinking speeds (e.g., McDonnell and Buesseler 2010, and references cited therein). Compact fecal pellets whether ovoid or cylindrical in shape will sink at a much faster speed through the water column than large amorphous and porous marine snow (Ebersbach et al. 2011). In this study, the separation of particles into fecal pellet-type particles and "others" (including plankton and marine snow) reveal interesting patterns. A surprising proportion of small fecal pellets was present even including the deepest layers (>4000 m). These small fecal pellets are usually not considered to contribute to a large portion of vertical flux (e.g., Guidi et al. 2008; their Fig. 5), and producers of these fecal pellets are hardly abundant enough to explain their high occurrence in the North Atlantic Deep Water or the Antarctic Bottom Water.

A Kolmogorov-Smirnov two sample test revealed that the frequency distributions of particles in the different water masses were significantly different in all but two comparisons (Table 1), supporting the general notion of a characteristic particle inventory for each of the water masses (Bochdansky et al. 2010). Since the K-S statistic is sensitive to both the shape and the location of the cumulative frequency distribution, it is a sensitive measure of whether or not two distributions come from the same statistical population. From Fig. 10, it is apparent that the proportion of fecal pellets in the size range of 50–100 μm is higher in the NADW than in the other two water masses above and below. The distribution of fecal pellets is heavily skewed toward smaller sizes in the deeper water masses (NADW & AABW, Fig. 10), while the size distribution of fecal pellets is more symmetrical in the AAIW. This may reflect the fact that smaller fecal pellets do not sink as fast and are fragmented and remineralized before they reach deeper waters. The mesopelagic (AAIW) on the other hand, is a habitat of many zooplankton species which continuously add new fecal pellets to the water (Steinberg et al. 2008).

Comments and recommendations

One possible step toward improving the current system is to use shorter wave lengths. We were limited to a red laser (640 nm) because the single mode fiber gave optimum light propagation and emission for red wavelengths, but soon shorter wavelength fibers are expected to become available. Since resolution increases linearly with a decrease in wavelength a blue laser of 447 nm with suitable fiber optics would improve resolution by 40%. However, there is a distinct advantage of using a red light over other wavelengths as very few plankton organisms are able to perceive it and thus are less likely to be attracted to, and aggregate in it.

Most of the 70 kg weight of this system was due to the 2 cm thick walls and the ca. 5 cm thick end-caps of the stainless steel housings. Housings can be produced much lighter if there is no need to deploy the instrument to depths of 6000 m. Alternatively, the housings could be manufactured of much lighter albeit more expensive titanium. The minimum inner diameter of one housing was dictated by the dimensions of the Axiomtek computer. Embedded computers continue to become smaller so that the diameter and thus the weight may be reduced further in the future. A modular design using different size housings for different components, and connecting them via fiber optics cables may also be a viable alternative to cut down on housing size and weight. The ability to run on standard operating systems such as Microsoft Windows or Ubuntu Linux adds greatly to the flexibility of this setup. This allows use with a wide variety of cameras and image-processing programs without the added expense of specialized software adaptation and hardware integration.

A complicated setup procedure had to be followed in order to integrate Streampix software and the JAI camera (the procedure can be obtained from the authors). More simple systems already exist that do not require the same level of customization. We highly recommend partitioning the hard drive into two parts: a small partition that operates the software of the camera, and a large partition that is solely used to store recorded images. A "quick reformat" of the image partition can thus be performed giving equal access to all sectors on the partition. This increases writing speed on the hard disk, and consequently, keeps the frame rate of recording at its maximum.

Copying videos through USB onto an external hard disk is time-consuming (in this setup approximately 10 h for a 2 h video), and using the GigE port for data transfer is more advisable. In some cases, it may be more practical to open the housing and switch out the whole computer between deployments if high frequency deployments are desired and deck operations allow it. If only one or two deployments are needed in 24 hours, or the videos are kept short (i.e., using a smaller

depth range), videos can also be downloaded through a bulkhead connector. The strands of the USB cables and VGA connectors could be separated and connected through a self-sealing pin connector (e.g., Subconn). Cat5e ethernet Suconn connectors have also become available recently. This is preferable where the DIHM remains on deck and is exposed to the elements, as is the case in most oceanographic expeditions. It should also be pointed out that massive storage capacity needs to be considered for the files and backup copies when contemplating high frequency deployments. For this expedition alone, we consumed a total of 10 TB with none of the space allocated for backups.

Higher shutter speeds of new digital cameras will certainly help in the reconstruction of particles < 50 μm at the typical speeds of CTD rosettes through the water. Cameras with 10 μs and shorter shutter speeds are already available on the market today. The use of nanosecond or microsecond pulsed lasers may also be an option but since they are expensive and the shutter of the camera would have to be synchronized with the laser pulses, a configuration like that would increase weight, complexity, and costs of this system considerably.

DIHM imaging at 7 frames s^{-1} and at a cage descent speed of 1 m s^{-1}, will generate 7,000 holograms per km depth. Furthermore, each hologram needs to be reconstructed in several planes to reveal all the organisms that were captured by the holograms. Development of methods for the automatic analysis of holograms will thus be essential for future DIHM imaging applications. One can distinguish three levels of analysis. 1) The selection from the complete hologram data set of only those holograms that actually contain objects. 2) The automatic determination of the in-focus planes of the objects that are reconstructed from these holograms with DIHM software, and 3) the automatic counting, sizing, and identification of all in focus organisms. Step 1 can be achieved by first selecting a hologram of an object-free sample volume as reference. A comparison of pixel intensity histograms for various holograms with the histogram of the reference can indicate the presence of objects. Step 2 can be achieved through edge detection algorithms together with object sizing methods and will be available through future Holosuite DIHM software upgrades. The automatic counting and sizing of in-focus objects for step 3 can be accomplished through intensity threshold adjustment of a reconstruction followed by object segmentation and image conversion to binary format. An object outline plot then allows a determination of the object area, contour length and the length and orientation of the major object axes. While the first two steps are already available in a variety of systems including the most recent Holosuite software (Resolution Optics), the most challenging goal of automatic object identification is the comparison of reconstructed DIHM objects with a library of images of typical plankton organisms. Great strides have been made recently for the automated identification of images taken with a variety of devices (e.g., Benfield et al. 2007; Gislason and Silva 2009;

Gorsky et al. 2010; Bachiller et al. 2012; Grosjean et al. 2012) and more are sure to come.

We believe that the DIHM as demonstrated here has the potential to become a routine instrument attached to CTD rosettes like fluorometers, transmissometers, or optical backscatter sensors are today, with the benefit of providing a permanent high-resolution record of small-scale distributions of plankton and other particles. Currently, the only standard instrument on a CTD rosette that measures a bulk biological property is the fluorometer, which provides a limited view of the ocean's biology. Considering the widely acknowledged role of plankton organisms in biogeochemical cycles, a record of plankton distributions linked to CTD data would be highly desirable. While it may be impossible to analyze the wealth of information of each deployment immediately, these holograms can be archived and mined later for specific organisms, or for changes in abundance of organisms and particles over time. In the future, more advanced automatic image reconstruction and detection will become available for particle counting, sizing, and taxonomic identification. The point-source DIHM, reminiscent of the camera obscura of the Renaissance, is elegant in its simplicity, and requires minimal experience to build and deploy, all of which makes it particularly suitable for routine applications on a variety of oceanographic platforms.

Acknowledgments

References

Bachiller, E., J. A. Fernandes, and X. Irigoien. 2012. Improving semiautomated zooplankton classification using an internal control and different imaging devices. Limnol. Oceanogr. Methods 10:1-9 [doi:10.4319/lom.2012.10.1].

Beers, J. R., C. Knox, and J. D. H. Strickland. 1970. A permanent record of plankton samples using holography. Limnol. Oceanogr. 15:967-969 [doi:10.4319/lo.1970.15.6.0967].

Benfield, M. C., and others. 2007. RAPID. Research on automated plankton identification. Oceanography 20:172-187 [doi:10.5670/oceanog.2007.63].

Black, K. S., H. Sun, G. Craig, D. M. Paterson, J. Watson, and T. Tolhurst. 2001. Incipient erosion of biostabilized sediments examined using particle-filed optical holography. Environ. Sci. Technol. 35:2275-2281 [doi:10.1021/es0014739].

Bochdansky, A. B., S. M. Bollens (2004) Relevant scales in zooplankton ecology: Distribution, feeding, and reproduction of the copepod *Acartia hudsonica* in response to thin layers of the diatom *Skeletonema costatum*. Limnol. Oceanogr. 49:625-636.

———, H. M. van Aken, and G. J. Herndl. 2010. Role of macroscopic particles in deep-sea oxygen consumption. Proc. Natl. Acad. Sci. 107:8287-8291 [doi:10.1073/pnas.0913744107].

Carder, K. L., R. G. Steward, and P. R. Betzer. 1982. In situ holographic measurements of the sizes and settling rates of organic particulates. J. Geophys. Res. 87:5681-5685 [doi:10.1029/JC087iC08p05681].

Carpenter, E. J., A. Subramaniam, and D. G. Capone. 2004. Biomass and primary productivity of the cyanobacterium *Trichodesmium* spp. in the tropical N. Atlantic ocean. Deep Sea Res. I 51:173-203 [doi:10.1016/j.dsr.2003.10.006].

Chervin, J. C., G. Syfosse, and J. M. Besson. 1994. Mechanical strength of sapphire windows under pressure. Rev. Sci. Instrum. 65:2719-2725 [doi:10.1063/1.1145206].

Davis, C. S., S. M. Gallager, M. S. Berman, L. R. Haury, and J. R. Strickler. 1992a. The Video Plankton Recorder (VPR): Design and initial results. Arch. Hydrobiol. BeiheftErgeb. Limnol. 36:67-81.

———, S. M. Gallager, and A. R. Solow. 1992b. Microaggregations of oceanic plankton observed by towed video microscopy. Science 257:230-232 [doi:10.1126/science.257.5067.230].

———, and D. J. McGillicuddy. 2006. Transatlantic abundance of the N2-fixing colonial cyanobacterium Trichodesmium. Science 312:1517-1520 [doi:10.1126/science.1123570].

Ebersbach, F., T. W. Trull, D. M. Davies, and S. G. Bray. 2011. Controls on mesopelagic particle fluxes in the sub-Antartic and polar frontal zones in the Southern Ocean south of Australia in summer—perspectives from free-drifting sediment traps. Deep Sea Res. II 58:2260-2276 [doi:10.1016/j.dsr2.2011.05.025].

Gabore, D. 1948. A new microscopic principle. Nature 161:777-778 [doi:10.1038/161777a0].

Gislason, A., and T. Silva. 2009. Comparison between automated analysis of zooplankton using ZooImage and traditional methodology. J. Plankton Res. 31:1505-1516 [doi:10.1093/plankt/fbp094].

Gorsky, G., and others. 2010. Digital zooplankton image analysis using the ZooScan integrated system. J. Plankton Res. 32:285-303 [doi:10.1093/plankt/fbp124].

Grosjean, P., and K. Denis. 2012. Zoo/PhytoImage version 1.2-0 Computer-assisted plankton image analysis. User's Manual. <www.sciviews.org/zooimage/>.

Graham, G. W., and W. A. M. Nimmo Smith. 2010. The application of holography to the analysis of size and settling velocity of suspended cohesive sediments. Limnol. Oceanogr. Methods 8:1-15 [doi:10.4319/lom.2010.8.1].

Gruber, N., and J. N. Galloway. 2008 An Earth-system perspective of the global nitrogen cycle. Nature 451:293-296 [doi:10.1038/nature06592].

L. Guidi, G. Gorsky, H. Claustre, J. C. Miquel, M. Picheral, and L. Stemmann (2008) Distribution and fluxes of aggregates >100μm in the upper kilometer of the South-Eastern Pacific. Biogeosciences, 5, 1361–1372.

Harris, D. C. 1992. Infrared window and dome materials (tutorial texts in optical engineering). Society of Photo Optical.

Heflinger, L. O., G. L. Stewart, and C. R. Booth. 1978. Holographic motion pictures of microscopic plankton. Appl. Optics 17:951-954 [doi:10.1364/AO.17.000951].

Jackson, G. A., R. Maffione, D. K. Costello, A. L. Alldredge, B. E. Logan, and H. G. Dam. 1997. Particle size spectra between 1um and 1 cm at Monterey Bay determined using multiple instruments. Deep Sea Res. I 44:1739-1767 [doi:10.1016/S0967-0637(97)00029-0].

Jericho, S., P. Klages, J. Nadeau, E. M. Dumas, M. H. Jericho, and H. J. Kreuzer. 2010. In-line digital holographic microscopy for terrestrial and exobiological research. Planetary and Space Science 58(4):701-705 [doi:10.1016/j.pss.2009.07.012].

Jericho, S. K., J. Garcia-Sucerquia, W. Xu, M. H. Jericho, and H. J. Kreuzer. 2006. Submersible digital in-line holographic microscope. Rev. Sci. Instrum. 77:0437061-10 [doi:10.1063/1.2193827].

Katz, J., P. L. Donaghay, J. Zhang, S. King, and K. Russell. 1999. Submersible holocamera for detection of particle characteristics and motions in the ocean. Deep- Sea Res. 46:1455-1481 [doi:10.1016/S0967-0637(99)00011-4].

Knox, C. 1966. Holographic microscopy as a technique for recording dynamic microscopic subjects. Science 153:989-990 [doi:10.1126/science.1123570].

Kreuzer, H. J., K. Nakamura, A. Wierzbicki, H. W. Fink, and H Schmid. 1992. Theory of the point source electron microscope. Ultramicroscopy 45:381-403 [doi:10.1016/0304-3991(92)90150-I].

LaRoche, J., and E. Breitbarth. 2005. Importance of the diazotrophs as a source of new nitrogen in the ocean. J. Sea Res. 53:67-91 [doi:10.1016/j.seares.2004.05.005].

Lewis, N. I., W. Xu, S. K. Jericho, H. J. Kreuzer, M. H. Jericho, and A. D. Cembella. 2006. Swimming speed of three species of Alexandrium (Dinophyceae) as determined by digital in-line holography. Phycologia 45:61-70 [doi:10.2216/04-59.1].

Malkiel, E., O. Alquaddoomi, and J. Katz. 1999. Measurements of plankton distribution in the ocean submersible holography. Meas. Sci. Technol. 10:1141-1152.

———, J. N. Abras, E. A. Widder, and J. Katz. 2006. On the spatial distribution and nearest neighbor distance between particles in the water column determined from in situ holographic measurements. J. Plankton Res. 28:149-170 [doi:10.1093/plankt/fbi107].

McManus, M. A., and C. B. Woodson. 2012. Review. Plankton distribution and ocean dispersal. J. Exp. Biol. 215:1008-1016 [doi:10.1242/jeb.059014].

McDonnell, A. M. P., and K. O. Buesseler. 2010. Variability in the average sinking velocity of marine particles. Limnol. Oceanogr. 55:2085-2096 [doi:10.4319/lo.2010.55.5.2085].

O'Hern, T. J., L. d' Agostino, and A. J. Acosta. 1988. Comparison of holographic and Coulter Counter measurements of cavitation nuclei in the ocean. J. Fluids Eng. 110:200-207 [doi:10.1115/1.3243535].

Perkins, R. G., H. Sun, J. Watson, M. A. Player, G. Gust, and D. M. Paterson. 2004. In-line laser holography and video analysis of eroded floc from engineered and estuarine sediments. Environ. Sci. Technol. 38:4640-4648 [doi:10.1021/es040011i].

Pfitsch, D. W., E. Malkiel, Y. Ronzhes, S. R. King, J. Sheng, and J. Katz. 2005. Development of a free-drifting submersible digital holographic imaging system. Proceedings of MTS/IEEE OCEANS 1:690- 696 [doi:10.1109/OCEANS.2005.1639833].

Schlitzer, R. 2011. Ocean Data View. <http://odv.awi.de>.

Sheng, J., E. Malkiel, and J. Katz. 2006. Digital holographic microscope for measuring three-dimensional particle distributions and motions. Appl. Optics 45:3893-3901 [doi:10.1364/AO.17.000951].

Sokolov, R. N., E. A. Kudryavitskiy, and G. D. Petrov. 1971. Submarine laser instrument for measuring the size spectra of particles suspended in sea water. Izv. Atmos. Ocean. Phys. 7:1015-1018.

Sosik, H. M., and R. J. Olson. 2007. Automated taxonomic classification of phytoplankton sampled with imaging-in-flow cytometry. Limnol. Oceanogr. Methods 5:204-216 [doi:10.4319/lom.2007.5.204].

Sun, H., D. C. Hendry, M. A. Player, and J. Watson. 2007. In situ underwater electronic holographic camera for studies of Plankton. IEEE J. Ocean. Eng. 32:373-382 [doi:10.1109/JOE.2007.891891].

Steinberg, D.K., B. A. S. Van Mooy, K. O. Buesseler, P. W. Boyd, T. Kobari, D. M. Karl (2008) Bacterial vs. zooplankton control of sinking particle flux in the ocean's twilight zone. Limnol. Oceanogr., 53:1327–1338.

Tomczak, M., and J. S. Godfrey. 2003. Regional oceanography: an introduction, 2nd ed. Butterworth-Heinemann.

Talapatra, S., and others. In press. Characterization of biophysical interactions in the water column, using in situ digital holography. Mar. Ecol. Prog. Ser.

Tyrrell, T., E. Maranon, A. J. Poulton, A. R. Bowie, D. S. Harbour, and E. M. S. Woodward. 2003. Large-scale latitudinal distribution of Trichodesmium spp. in the Atlantic Ocean. J. Plankton Res. 25:405-416 [doi:10.1093/plankt/25.4.405].

Vikram, C. S. 1992. Particle field holography. Cambridge Univ. Press [doi:10.1017/CBO9780511524196].

Watson, J. 2005. Underwater holography—past and future. Proc. SCIE. 6252:1-10 [doi:10.1117/12.677172].

———, and others. 2003. A holographic system for subsea recording and analysis of plankton and other marine particles (HOLOMAR). Oceans Proc. 2:830-837 [doi:10.1109/OCEANS.2003.178428].

Wu, J., W. Sunda, E. A. Boyle, and D. A. Karl. 2000. Phosphate depletion in the Western North Atlantic Ocean. Science 289:759-762 [doi:10.1126/science.289.5480.759].

Xu, W., M. H. Jericho, I. A. Meinertzhagen, and H. J. Kreuzer. 2001. Digital in-line holography for biological applications. Proc. Natl. Acad. Sci. 98(20):11301-11305 [doi:10.1364/AO.17.000951].

———, ———, ———, and ———. 2002. Digital in-line holography of microspheres. Appl. Opt. 41:5367-5375 [doi:10.1364/AO.41.005367].

———, ———, H. J. Kreuzer, and I. A. Meinertzhagen. 2003. Tracking particles in four dimensions with in-line holographic microscopy. Optic Lett. 28(3):164-166 [doi:10.1364/OL.28.000164].